ADVANCED FUNCTIONAL MATERIALS

Supporting Information

for *Adv. Funct. Mater.*, DOI: 10.1002/adfm.201606717

Thickness Dependent Properties in Oxide Heterostructures Driven by Structurally Induced Metal–Oxygen Hybridization Variations

Zhaoliang Liao, Nicolas Gauquelin, Robert J. Green, Sebastian Macke, Julie Gonnissen, Sean Thomas, Zhicheng Zhong, Lin Li, Liang Si, Sandra Van Aert, Philipp Hansmann, Karsten Held, Jing Xia, Johan Verbeeck, Gustaaf Van Tendeloo, George A. Sawatzky, Gertjan Koster, Mark Huijben, and Guus Rijnders*

Supporting Information

Thickness dependent properties in oxide heterostructures driven by structurally induced metal-oxygen hybridization variations

Zhoaliang Liao, Nicolas Gauquelin, Robert J. Green, Sebastian Macke, Julie Gonnissen, Sean Thomas, Zhicheng Zhong, Lin Li, Liang Si, Sandra Van Aert, Philipp Hansmann, Karsten Held, Jing Xia, Johan Verbeeck, Gustaaf Van Tendeloo, George A. Sawatzky, Gertjan Koster, Mark Huijben*, Guus Rijnders

1. Measurement of B-O-B bond angle

Using statistical parameter estimation theory,[1-3] the 2D coordinates of each atomic column of the $La_{2/3}Sr_{1/3}MnO_3$ (LSMO) on $NdGaO_3$ (NGO) (110) heterostructure have been determined from the Annular Bright Field scanning transmission electron microscopy (ABF-STEM) image shown in Fig. S1a. Therefore, a parametric model in which projection images of the atomic columns are described using Gaussian peaks has been assumed. The parameters of this model, including the positions, height, and width of the intensity peaks, were determined using the least-squares estimator. The refined model evaluated at these estimated parameters is shown in Fig. S1b. From the estimated positions of the oxygen and B site (Ga or Mn) atomic columns, as indicated in the right top corner of Fig. S1b, the B-O-B bond angle has been calculated. The result for the averaged B-O-B angle in every atomic layer is shown in Fig. 1b in the main text.

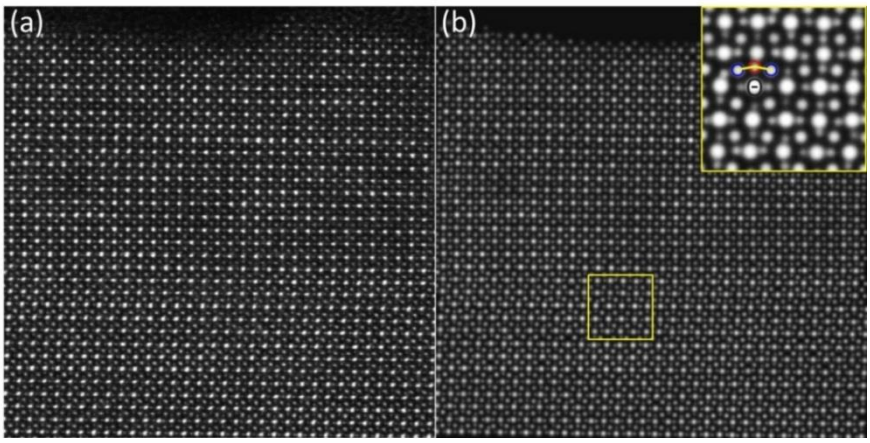

Figure S1: (a) Inversed ABF-STEM image of a 20 unit cells LSMO film on NGO (110) substrate. (b) Refined parametric model using statistical parameter estimation. Inset at right-top corner shows the zoom-in image of red square region.

2. Characterization of lattice parameters

The lattice constant of LSMO films was measured by PANalytical-X'Pert Materials Research Diffractometer (MRD) at high resolution mode. Figure S2a shows the θ-2θ scan of different thickness of LSMO with/without 6 unit cells (uc) $SrTiO_3$ (STO) buffer layers. The out-of-plane lattice constant ***c*** is extracted from the position of LSMO $(002)_{pc}$ peak as indicated by the arrow. Here subscript pc represents pseudocubic indices. As shown in Fig. S2a, the 6 uc STO buffered 30 uc LSMO film (L_{30}/S_6) has lower peak position than non-buffered 30 uc LSMO (L_{30}), but is almost the same with 90 uc LSMO film (L_{90}). The unit cell lattice parameters (***a***, ***b***, ***c***) were further determined by reciprocal space mapping (RSM) of LSMO $(240)_{pc}$, $(-240)_{pc}$, $(024)_{pc}$, $(0\text{-}24)_{pc}$ peaks.[4] Here, we only shows $(204)_{pc}$ peaks as examples in Fig. S2b. Using the q_z value of the $(204)_{pc}$ peak, the lattice constant ***c*** can be determined from formula $\boldsymbol{c}=4/q_z$. According to RSM, both the LSMO and STO layers are fully strained to NGO substrate, thus the LSMO and STO share the same in-plane lattice constant with NGO. RSM also illustrates that the L_{30}/S_6 film has lower q_z and therefore bigger out-of-plane lattice constant ($\boldsymbol{c}=4/q_z$) than non-buffered LSMO (L_{30}). In contrast to the STO buffer effect, the capping of 9 uc STO on top of LSMO (S_9/L_{30}) does not influence the LSMO lattice constant (see Fig. S2b**)**. For thinner films, e.g., 15 uc LSMO film, it is hard to determine peak position in θ-2θ scan, but the ***c*** can be measured from RSM. From the reciprocal space mapping, we can also determine the peak width and therefore estimate the uncertainty of the lattice parameter. According to the RSM and the θ-2θ scan, the lattice constant ***c*** for different LSMO films and their uncertainties are obtained.

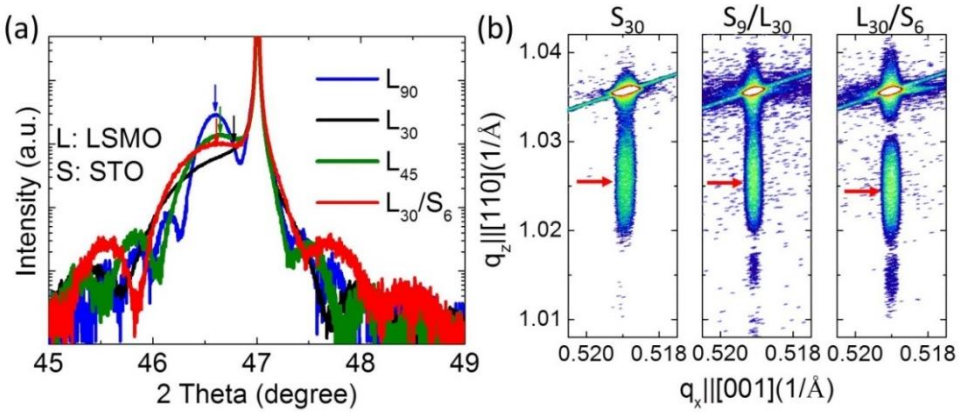

Figure S2: (a) θ-2θ scan of different thickness of LSMO with or without 6 uc STO buffer layers. The arrows indicate LSMO $(002)_{pc}$ peak positions. (b) RSM of $(204)_{pc}$ peaks of 30 uc LSMO films with/without STO buffer or capping layer. The red arrows indicate the LSMO peak positions. L and S represent LSMO and STO respectively, which are used for other figures as well.

3. The ABF-STEM image of STO buffered LSMO film

The ABF image of 6 uc STO buffered LSMO (L_{30}/S_6) film on NGO (110) substrate is shown in Fig. S3a-b. The tilt present in NGO quickly decays into the STO and is almost absent in the second STO unit cell already, similarly as previously observed for L_6/S_9.[5] The LSMO which is now connected to non-tilt STO layer presents no octahedral tilt. Figure S3b highlights the BO_6 octahedra across the LSMO/STO interface where the significantly reduced tilt angle is observed and compared with non-buffered LSMO film as showed in Fig. 1a in the main text.

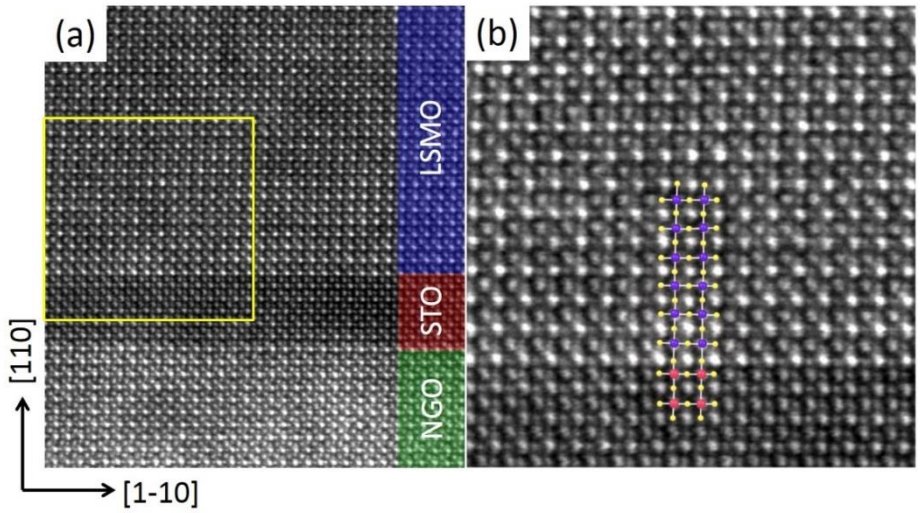

Figure S3: (a) ABF-STEM image of a 6 uc STO buffered 30 uc LSMO film. (b) Zoom-in of the yellow square region in (a). The colorized atom and bond highlight the octahedra across interface.

4. Patterned growth of STO and LSMO layers

By using shadow mask during growth, the film can be patterned as shown in Fig. S4. For the patterned LSMO sample, a shadow mask was first used to block one side of the NGO substrate during the growth of a STO buffer layer. Subsequently, a LSMO layer was deposited without shadow mask. The final step was to grow a STO capping layer with a shadow mask. This process produced three different regions—LSMO/NGO, LSMO/STO/NGO and STO/LSMO/NGO on the same substrate. The thicknesses of the STO and LSMO layers were monitored by reflection high energy electron diffraction (RHEED) intensity oscillations during growth.

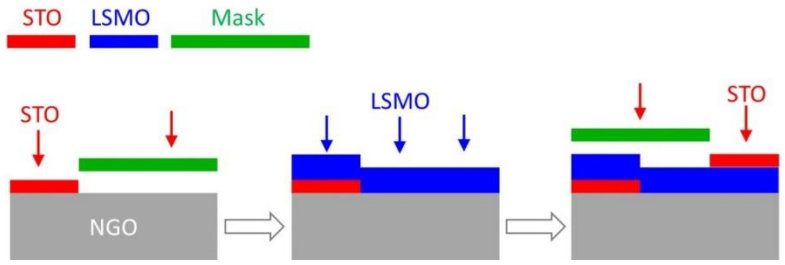

Figure S4: Process of patterned growth of STO and LSMO layers.

5. Determination of T_C from Kerr measurement

To determine the Curie temperature (T_C), the patterned LSMO sample was cooled below Curie temperature using a liquid-helium-cooled cryostat in a magnetic field of 2000 gauss which will cant the magnetization along out-of-plane direction. The Kerr signal was measured by a Sagnac interferometer and the T_C was determined from the second derivative of Kerr signal versus temperature as shown in Fig. S5. Since the magnetization easy axis is in-plane, applying a magnetic field to tilt the magnetization out of plane will have an effect of softening the paramagnetic to ferromagnetic phase transition, leading to less sharp transition in Kerr signal. However, the second derivative can largely amplify the transition and thus be used to determine the Curie temperature. As shown in Fig. S5, The T_C is determined as the temperature point where the value of second derivate of Kerr signal reaches maximum negative value. There is a 1 K uncertainty in T_C due to the signal noise associated with differentiating twice. Although this is an uncommon method of determining the T_C, but it still allows a quantitative comparison between the relative transition temperatures of different regions. Furthermore, the T_C from Kerr measurement agrees well with the value measured by vibrating sample magnetometry (VSM), indicating a good estimation of T_C using second derivate of Kerr signal.

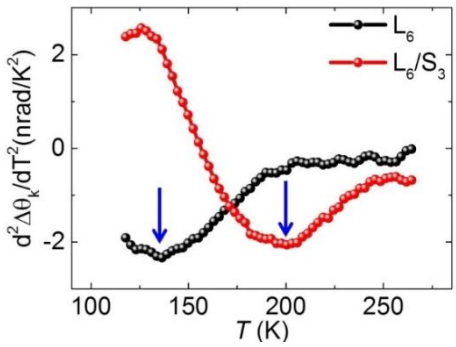

Figure S5: Second derivative of Kerr signal versus temperature for different regions of a patterned LSMO film mentioned in Fig. 2 in main text. Arrows indicate the Curie temperature.

6. Experimental and simulated RSXR Data

The chemical depth profiles of different LSMO samples have been determined from reflectivity curves measured at off-resonant energies, utilizing the optical contrast before and after each resonance. The film thickness, roughness, and a small contamination of light elements (such as oxygen and carbon) were taken as fit parameters, while the concentrations

of the NGO, STO, and LSMO elements were fixed at stoichiometric values. Figure S6 shows the corresponding measurements and fits performed by the software ReMagX.[6,7] After determining the chemical profile, further measurements and modeling were used to determine the magneto-optical depth profile. For these measurements, a permanent magnet array producing a homogenous 0.6 Tesla field was inserted in the sample environment, aligning the magnetization in the film in-plane along the measurement scattering plane. Two different reflectivity curves at the Mn L_3 resonance were measured by using left R_l and right circular R_r polarized light. The bottom panel of each subfigure in Fig. S6 shows the asymmetry defined as $A = (R_l-R_r)/(R_l+R_r)$ and the corresponding fit. During fitting, the magnetic depth profile was assumed to be one homogeneous magnetic layer with in-plane magnetization and free thickness, position and magnetic roughness. As model inputs, the magneto optical constants were determined by the XMCD spectra taken from [8].

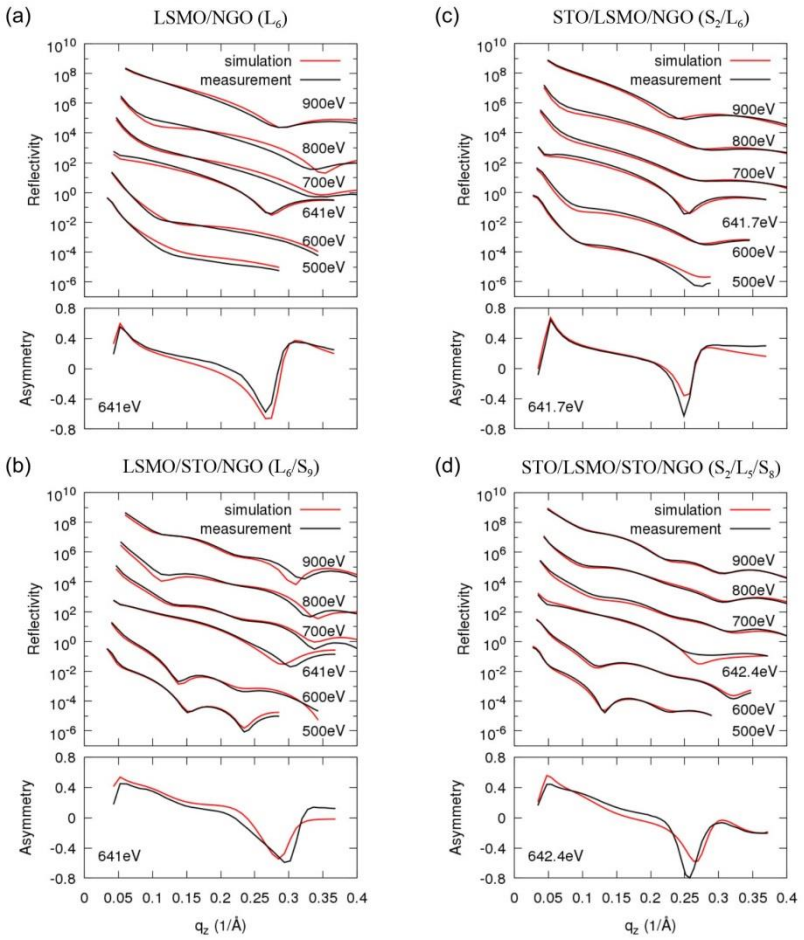

Figure S6: Experimental and simulated RSXR data. The data shown for the four samples correspond to the four extracted profiles in Fig. 3 of the main text. The upper panel for each sample contains q_z-scans at the specified energies using polarized light. The lower panel contains asymmetry spectra, obtained from the difference between left and right circular polarized light divided by the sum of both.

7. DFT calculation of structural effect on orbital hybridization

The impact of octahedral tilt on the electronic structure of LSMO is investigated using first principles density functional theory (DFT) calculations. The atomic relaxations are carried out with the VASP code[9,10] by using Projector augmented-wave (PAW) method.[11] Subsequently the electronic structure calculations were performed by using the WIEN2K code[12] with full-potential linearized augmented plane-wave method.[13] In both codes the generalized gradient approximation (GGA) of Perdew, Burke, and Ernzerhof (PBE)[14] functional was adopted to treat the exchange-correlation functions. The Sr doping in $LaMnO_3$ bulk ($La_{0.67}Sr_{0.33}MnO_3$) system is realized by using the virtual crystal approximation.

To study the effect of MnO_6 octahedral tilting, three different structures are considered in our study: cubic, $GdFeO_3$ (GFO)-type and NGO-type. For the cubic structure, there is no octahedral tilting, the Mn-O-Mn bond angle is 180^o. The GFO- and NGO-type structures are those of LSMO but adopted to the GFO and NGO orthorhombic distortion, with NGO-type having larger octahedral tilting. In order to summarize the effects of the change of Mn-O-Mn bond angle and Mn-O bond length on the LSMO electronic structure, two group of calculations are carried out: In the first group (Group-I) we keep the Mn-O bond length constant. In this way any effect from Mn-O bond length is excluded, only the bond angle is changed (and subsequently the lattice parameters). In the second group (Group-II) we keep the Mn-Mn distance constant but otherwise relax the structure, rotating the MnO_6 octahedron in the xy plane and tilting them along the Z direction. This yields the GFO-type as an energy minimum; for the NGO-type we enhance the Mn-O-Mn angle according to the experimental NGO structure. Thus in the process of rotation and tilting the Mn-O bond length is also increased for Group-II calculations. By this confinement we can investigate the effect from both Mn-O-Mn bond angle and Mn-O bond length separately. All the structural parameters are summarized in Table S1. The half-metal ferromagnetic state of LSMO system is already obtained even without considering electron correlation, e.g. from DFT+U or DFT+DMFT methods. We also test the robustness of our results using a reasonably large interaction U in DFT+*U* calculations: no remarkable change occurs. To include the effect of octahedral rotation and tilting, a $\sqrt{2}\times\sqrt{2}\times2$ supercell (20 atoms) was used in our electron structure calculations of the density of states (DOS) and bandwidth.

Table S1: Summary of structural parameters (lattice constants, Mn-O-Mn angles and Mn-O bond length). We consider three crystal structures (cubic, GFO- and NGO-type) and either keep the Mn-O bond length constant (Group-I) or the Mn-Mn distance constant of the crystal structure (Group-II).

Group-I: Mn-O constant								
Structure	a(Å)	b(Å)	c(Å)	Mn-O-Mn angle θ (degree)			Mn-O bond (Å)	
				θ_{xy}	θ_z	<θ>	xy	z
Cubic	3.848	3.848	3.848	180	180	180	1.924	1.924
GFO-type	3.834	3.793	3.810	162.8	162.8	162.8	1.924	1.924
NGO-type	3.829	3.633	3.771	151.6	151.2	151.5	1.924	1.924
Group-II: Mn-Mn constant								
Structure	a(Å)	b(Å)	c(Å)	Mn-O-Mn angle (degree)			Mn-O bond (Å)	
				θ_{xy}	θ_z	<θ>	xy	z
Cubic	3.848	3.848	3.848	180	180	180	1.924	1.924
GFO-type	3.848	3.848	3.848	159.4	160.5	159.9	1.952	1.953
NGO-type	3.848	3.848	3.848	151.6	151.2	151.5	1.984	1.987

Figure S7a shows an example of the orbital-resolved density of states (DOS) for cubic LSMO ($\theta = 180^o$) from which we can extract the bandwidth of the 3d majority e_g and t_{2g} orbitals, which is 4.83 eV and 3.336 eV, respectively. The DOS appearing at -7.5 eV to -4eV region arises from hybridization between oxygen 2p and Mn 3d orbitals and is excluded when calculation the bandwidth. By decreasing the bond-angle without changing the Mn-O bond length from 180^o (cubic-type), 162.8^o (GFO-type) to 151.5^o (NGO-type) the effect of bond-angle on the electronic structure of LSMO (Group-I) is shown in Fig. S7b-c. There is a valley around -1 eV for the total DOS as shown in Fig. S7b, above and below which the DOS mainly comes from e_g and t_{2g}, respectively. In cubic LSMO, the bandwidth of both t_{2g} and e_g are so big that the t_{2g} and e_g bands overlap, but their overlap is getting smaller with increasing the octahedral tilting (or said reducing bond angle) as shown in Fig. S7b. In NGO-type LSMO, the bandwidths of both t_{2g} and e_g become narrower. As a result a gap opens between t_{2g} and e_g orbital (zero DOS at the valley Fig. S7b). Figure S7c shows the partial DOS of majority e_g orbital, clearly demonstrating the narrowing of the e_g band with decreasing bond-angle.

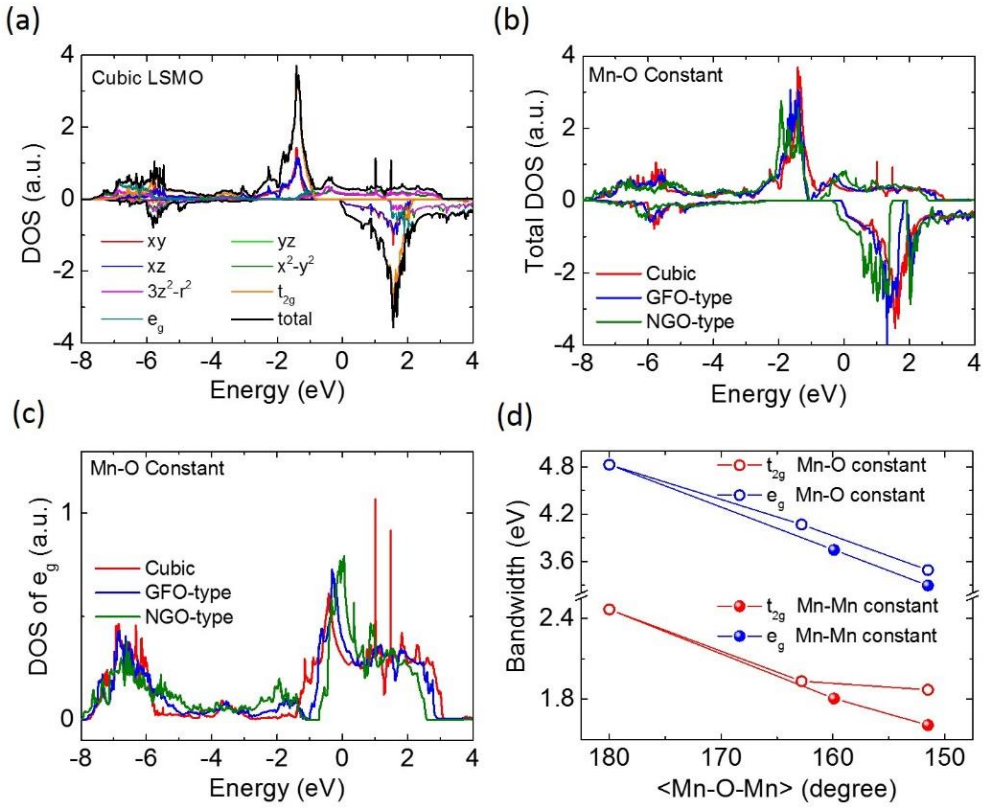

Figure S7: Octahedral tilt effect on bandwidth. (a) Calculated orbital- and spin-resolved DOS for both e_g and t_{2g} orbitals for cubic LSMO. **(b)** Spin-resolved total DOS and **(c)** majority e_g DOS orbital of LSMO comparing cubic to GFO- and NGO-type of distortion with constant Mn-O bond length (Group-I). **(d)** Bandwidth as a function of tilting angle for both, constant Mn-O bond length (Group-I) and constant Mn-Mn distance (Group-II).

The bandwidth versus bond-angle is plotted in Fig. S7d. The bandwidths of both t_{2g} and e_g decrease with decreasing bond angle, e.g., in cubic LSMO the e_g bandwidth is 4.83 eV, while it is 3.491 eV for NGO-type LSMO. Therefore, reducing the bond angle from 180^o to 151.5^o results in a 28% reduction of bandwidth. Since the oxygen 2p orbital points towards the e_g orbital lobes not to those of the t_{2g} orbitals, the e_g orbitals have larger bandwidth as well as a larger the bandwidth reduction in Fig. S7d. Figure S7d also shows the calculated bandwidth of three different LSMO structures from Group-II where we keep the Mn-Mn distance constant but change the bond angle. The bandwidth is again reduced with decreasing bond angle, similar to our finding in Group-I LSMO. However, differently from Group-I, the bandwidth of Group-II LSMO gets narrower more quickly as the bond angle is reduced (see Fig. S7d). The bandwidth of e_g is reduced by 32% when the bond angle changes from 180^o to 151.5^o for a constant Mn-Mn distance. That is, both the elongated Mn-O bond and the increased octahedral tilt reduce the bandwidth cooperatively. Therefore, the effect of octahedral tilt on bandwidth reduction will be enhanced somewhat if the Mn-Mn distance

instead of the Mn-O bond length is locked. Taken together, both calculations show that the main driver behind the reduced bandwidth is the tilting of the Mn-O-Mn angle in the distorted structure.

The octahedral tilt will dominate the orbital hybridization in bulk LSMO, but the surface structure reconstruction will also play an important in determining the surface electronic structure of LSMO. To investigate the surficial structure relaxation, DFT calculation of the structure of 1 uc LSMO was performed. For simplicity, the MnO_6 octahedral tilt is eliminated, i.e., cubic structure is adopted in this calculation. By fixing the in-plane lattice constant while freeing the out-of-plane lattice and all atomic positions, the out-of-plane lattice constant $\boldsymbol{c}_{film}^{relax}$ which is defined as Sr-Sr bond length is found to be 3.423 Å, only 88.9% of that the original non-relaxed unit cell (3.848 Å). This dramatic lattice compression is due to that the $(La_{2/3}Sr_{1/3}O)^{+0.67}/(MnO_2)^{-0.33}/(La_{2/3}Sr_{1/3}O)^{+0.67}$ system is polar and the intrinsic charge attractive force will push layers closer. Besides the Sr-Sr compression, the second feature of the film structure is that the distance between M and O at surface LaSrO layer is 2.07 Å, which is larger than the original 1.924 Å. The elongated M-O distance will dramatically reduce surfacial O-p to Mn-d hybridization.

The DFT calculation of 1 uc LSMO sandwiched between two STO layers which are both 2 uc thick was performed to investigate the impact of STO capping layer on the LSMO surface structure. It is found that the lattice constant $\boldsymbol{c}$ of STO sandwiched LSMO film becomes 3.719 Å and the Mn-O distance is 1.934 Å, both of which are very close to the original bulk values of 3.848 Å and 1.904 Å. Our DFT calculation indicates that the STO capping layer can reduce the surface structure distortion, explaining the experimental observation of the recovery of surface magnetism due to the presence of STO capping layer as shown in Fig. 2 and Fig. 3 in main text.

8. Valence profile in LSMO films

The change of valence is another effect that can vary the Curie temperature. The X-ray absorption spectroscopy (XAS) as shown Fig. 4b of main text already indicates a nearly identical Mn valence in different LSMO films. The XAS also indicates a Mn^{2+} peak located at ~ 640 eV. Regarding the fact that XAS detects near surface ~6 nm region, the presence of Mn^{2+} in 90 uc (= 35 nm) LSMO film then can only arise from surface region.[15,16] Such surficial Mn^{2+} may also degrade the surface magnetism and contribute the surface dead layer.

The layer resolved valence profile is acquired from STEM electron energy loss spectroscopy (STEM-EELS). Figures S8a-b show the layer resolved EELS of Mn $L_{2,3}$ edge of L_{30} and

L_{30}/S_6 films, respectively. Very small shifts of the peaks are observed. For the LSMO/NGO sample, the interfacial Mn peak position is shifted a little to higher energy, suggesting a slightly higher Mn valence in relative to bulk region. For the STO buffered LSMO film (L_{30}/S_6), the peak position of interfacial layer moves a little bit to lower energy, suggesting slightly lower Mn valence compared to the bulk region.

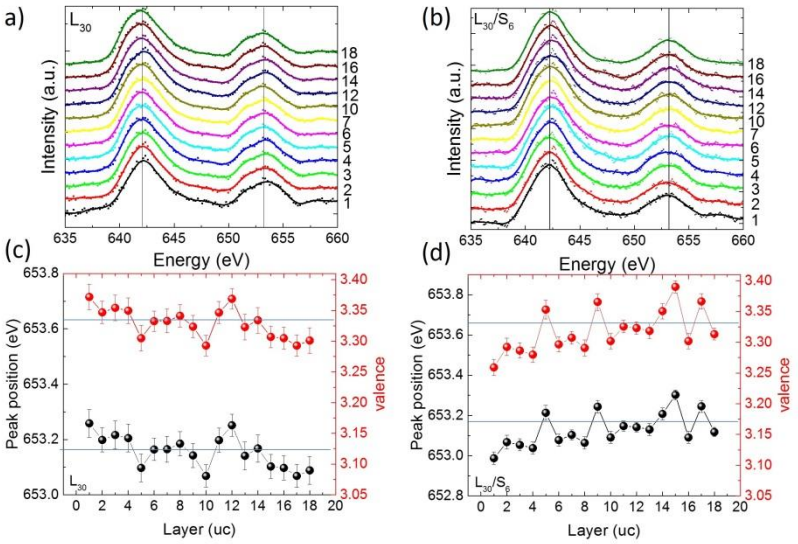

Figure S8: Valence profile in LSMO films. Layer resolved EELS of Mn $L_{2,3}$ peak across interface for (a) L_{30} (a) and (b) L_{30}/S_6 and corresponding Mn L_2 peak position and estimated valence profile for (c) L_{30} and (d) L_{30}/S_6.

According to previous reports by Mundy *et al.* [17] and Pellegrin *et al.* [18], the Mn $L_{2,3}$ peak position (E) is nearly linearly to Mn valence (x) and $t = \Delta x/\Delta E = \sim 0.42\ ev^{-1}$. With this slope t, the valence is estimated by the formula $x = 3.33+(E-E(3.33))\times t$ and resultant estimated valence profile is shown in Fig. S8c-d. The change of valence Δx is smaller than 0.1 for both interfaces. The interfacial Mn layer has a little lower valence at LSMO/STO interface in comparison to a little higher valence at LSMO/NGO interface. Such trend agrees with the polar catastrophe model reported by Mundy et al. [17]. We would like to emphasize that the peak positions are more precisely determined from XAS which indicates nearly identical valence in different samples while the EELS has higher noise level which will lead to uncertainty of determining a precise peak position and thus may overestimate the change of valence. Although a more occupancy of Mn e_g orbital will lead to a reduction of pre-edge intensity, but it is not significant that $I(Mn^{3+})/I(Mn^{4+}) = 0.8$.[19] Therefore, a much smaller change of pre-edge intensity will occur for a small change of valence and won't result to our observed pre-edge intensity profile. What is more, the Mn valence profile is expected to give rise to a little higher pre-edge intensity at the interface of LSMO/NGO, which is opposite to

experimental observation that much lower intensity of pre-edge is observed for interfacial layer. While for LSMO/STO/NGO, a uniform pre-edge intensity is observed. Furthermore, local charge transfer won't play a role in thick film (e.g., L_{30}), hence a reassembled bulk like O-K edge and an increased T_C due to STO buffer layer in 30 uc LSMO (L_{30}/S_6 vs. L_{30}) strongly suggest a central role of structure variation and resultant change of orbital hybridization in thickness driving phase transition.

9. Full spectra of O-K edge

XAS of oxygen K-edge was measured with the photon polarized along [001] axis of NGO. The full spectra of O-K edge for different LSMO films are shown in Fig. S9. The normalization of the spectra was done according to the total oxygen edge jump (i.e. scaled so that the pre- and post-edges were identical for all samples). This effectively normalizes to total oxygen content, allowing us to get a comparison between different samples. But for very thin films where the substrates start to make some contribution, it becomes very difficult to directly compare the intensity, but the line shapes still provide useful information for analyzing the characteristics of pre-edges, as discussed in main text.

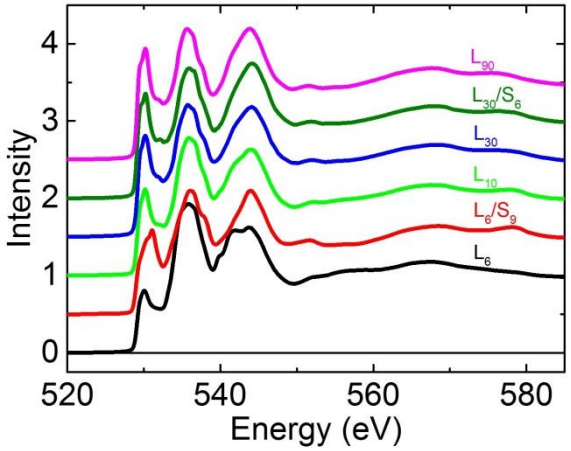

Figure S9: Full spectra of O-k edge for different LSMO samples with/without STO buffer layers.

References:

[1] A.J. den Dekker, S. Van Aert, A. van den Bos and D. Van Dyck, Maximum likelihood estimation of structure parameters from high resolution electron microscopy images. Part I: A theoretical framework, *Ultramicroscopy* **104**, 83 (2005).

[2] S. Van Aert, A.J. den Dekker, A. van den Bos, D. Van Dyck and J.H. Chen, Maximum likelihood estimation of structure parameters from high resolution electron microscopy images. Part II: A practical example, *Ultramicroscopy* **104**, 107 (2005).

[3] S. Van Aert, J. Verbeeck, R. Erni, S. Bals, M. Luysberg, D. Van Dyck, G. Van Tendeloo, Quantitative atomic resolution mapping using high-angle annular dark field scanning transmission electron microscopy, *Ultramicroscopy* **109**, 1236-1244 (2009).

[4] A. Vailionis, H. Boschker, W. Siemons, E.P. Houwman, D.H.A. Blank, G. Rijnders, G. Koster, Misfit strain accommodation in epitaxial ABO_3 perovskites: Lattice rotations and lattice modulations, *Phys. Rev. B* **83 (6)**, 064101 (2011).

[5] Z. Liao, M. Huijben, Z. Zhong, N. Gauquelin, S. Macke, R.J. Green, S.V. Aert, J. Verbeeck, G.V. Tendeloo, K. Held, G.A. Sawatzky, G. Koster, G. and G. Rijnders, Controlled lateral anisotropy in correlated manganite heterostructures by interface-engineered oxygen octahedral coupling, *Nature Mater*. **15(4),** 425 (2016).

[6] C. Chantler, Theoretical form-factor, attenuation and scattering tabulation for Z=1-92 from E=1-10 eV to E=0.4-1.0 MeV, *Journal of Physical and Chemical Reference Data* **24**, 71 (1995).

[7] website: www.remagx.org.

[8] C. Aruta, G. Ghiringhelli, V. Bisogni, L. Braicovich, N.B. Brookes, A. Tebano, and G. Balestrino, Orbital occupation, atomic moments, and magnetic ordering at interfaces of manganite thin films, *Phys. Rev. B* **80**, 014431 (2009).

[9] G. Kresse and J. Hafner, Ab initio molecular dynamics for liquid metals, *Phys. Rev. B* **47**, 558(R) (1993).

[10] G. Kresse and J. Furthmüller, Efficiency of ab-initio total energy calculations for metals and semiconductors using a plane-wave basis set, *Comput. Mater. Sci.* **6**, 15 (1996).

[11] P. E. Blöchl, Projector augmented-wave method, *Phys. Rev. B* **50**, 17953 (1994).

[12] P. Blaha, K. Schwarz, G. Madsen, D. Kvasnicka and J. Luitz, *WIEN2k*, An Augmented Plane Wave + Local Orbitals Program for Calculating Crystal Properties (Karlheinz Schwarz, Techn. Universität Wien, Austria), 2001. ISBN 3-9501031-1-2.

[13] D.J., Singh and Nordstrom, P. Lars, Pseudopotentials, and the LAPW method, Springer Science & Business Media (2006).

[14] J.P. Perdew, K. Burke, and M. Ernzerhof, Generalized gradient approximation made simple, *Phys. Rev. Lett.***77**, 3865 (1996).

[15] M. P. de Jong, I. Bergenti, V. A. Dediu, M. Fahlman, M. Marsi, and C. Taliani, Evidence for Mn^{2+} ions at surfaces of $La_{0.7}Sr_{0.3}MnO_3$ thin films, *Phys. Rev. B* **71**, 014434 (2005).

[16] J.-S. Lee, D.A. Arena, P. Yu, C.S. Nelson, R. Fan, C.J. Kinane, S. Langridge, M.D. Rossell, R. Ramesh and C.-C. Kao, Hidden magnetic configuration in epitaxial $La_{1-x}Sr_xMnO_3$ films, *Phys. Rev. Lett.* **105**, 257204 (2010).

[17] J.A. Mundy, Y. Hikita, T. Hidaka, T. Yajima, T. Higuchi, H.Y. Hwang, D.A. Muller and L.F. Kourkoutis, Visualizing the interfacial evolution from charge compensation to metallic screening across the manganite metal–insulator transition, *Nature Commun.* **5**, 3464 (2014).

[18] E. Pellegrin, L.H. Tjeng, F.M.F. de Groot, R. Hesper, G.A. Sawatzky, Y. Moritomo, and Y. Tokura, Soft X-Ray Magnetic circular dichroism study of the colossal magnetoresistance compound $La_{1-x}Sr_xMnO_3$, *J. Electron. Spectrosc. Relat. Phenom.* **86**, 115 (2013).

[19] J. Verbeeck, O. I. Lebedev, G. Van Tendeloo, J. Silcox, B. Mercey, M. Hervieu and A. M. Haghiri-Gosnet, Electron energy-loss spectroscopy study of a $(LaMnO_3)_8(SrMnO_3)_4$ heterostructure, *Appl. Phys. Lett.* **79**, 2037 (2001).